Park *et al.*
International Journal of Geo-Engineering (2024) 15:22
https://doi.org/10.1186/s40703-024-00223-3

International Journal of Geo-Engineering

RESEARCH Open Access

Experimental study on the effect of surface-projected conditions on the mechanical behavior of pile embedded in sand

Suhyuk Park[1], Gi-Yun Kim[1] and Ilhan Chang[1*]

*Correspondence:
ilhanchang@ajou.ac.kr

[1] Department of Civil Systems Engineering, Ajou University, Suwon 16499, Korea

Abstract

Surface-projected piles, such as helical and under-reamed piles, are widely utilized in geotechnical engineering to enhance the load-carrying capacities of pile structures with surface projection part. Despite the use of a wide variety of surface-projected conditions, detailed investigations considering various dimensions and angles of surface-projected piles remain limited in the current literature. This study aims to assess the effects of surface-projected widths w_p (10 mm, 20 mm, 40 mm) and angles θ (18°, 27°, 45°, 90°) on pile penetration resistance using a two-dimensional model and PIV analysis. Wider projections increased resistance, with a maximum of 1.84 kN—57% higher than conventional piles in the model ground. Penetration resistance was proportional to width at 90°; for $w_p = 20$ mm, penetration resistance decreased with increasing θ, while for $w_p = 40$ mm, it increased. Theoretical ultimate bearing capacity calculations emphasize differences from experimental results due to neglected shaft friction. Residual penetration resistance and particle displacement were observed for w_p of 20 mm and 40 mm after failure. This study provides insights into optimizing surface-projected pile design and understanding ground failure mechanisms.

Keywords: Penetration resistance, Surface-projected pile, PIV, Failure mechanism

Introduction

Pile structures are the most common foundation type applied in geotechnical engineering practices, where piles mainly transfer and resist overlaying structural loads with the combination of tip bearing and side friction [44, 57, 61, 62]. Since 1900s, several attempts have been conducted to increase the bearing capacity of foundations by modifying the base shape (e.g., shell footing or footing with skirt) of footing [8, 21, 29]. As the area of the foundation in contact with the soil increases, so does the load carrying capacity of the foundation. In the case of pile foundations, under-reamed pile or enlarged pile consists of one or more projected sections (i.e., bulbs) near the pile's base, increasing the surface area of a specific part (e.g., under-reamed pile, belled pile, waveform pile) along

the pile [11, 13, 31]. Deep foundations, like shallow foundations, increase the bearing capacity of the pile by increasing the part of the pile that is in contact with the soil. The economic advantage of using a surface-projected foundation is that fewer foundations can be installed, or the length of the foundation can be shortened. The influence of base diameters and angles on the uplift behavior was investigated using a centrifuge [15, 16]. Under-reamed piles have a higher pull–out resistance and bearing capacity than conventional piles owing to the passive resistance induced by the projected sections [39–41]. In addition, under-reamed pile reduces the vertical movement of the pile especially for expansive soils [1, 33]. The embedment length, projected section distance from the base, undrained cohesion, number of surface projections, spacing of surface projection, and projection diameter affect the load behavior of an under-reamed pile [1, 39–41]. The ground behavior caused by the vertical displacement of an under-reamed pile has also been studied via various methods. Sakr et al. [49] demonstrated increased pullout capacity and decreased vertical displacement of under-reamed piles in soils with various relative densities [49].

Various numerical analysis methods have been used to study the failure mechanism of the ground based on the displacement of the under-reamed pile [22, 23, 27, 33, 35, 36, 39, 39, 40, 40, 41, 41, 65]. Studies have found that considerable shearing occurs around the pile shaft and projected section [35], and that the soil movement induced by the pull-out of the belled pile occurs more around the projections than around the shaft [27].

The forms of the projected sections of the pile affect the bearing capacity. The angle of a belled shaft is generally 30° to 45°, in consideration of economic efficiency [14]. Using the finite element method, it has been confirmed that the maximum uplift capacity occurs when the extended angle is 45° [22]. To prevent punching of the projected section, a projected angle can be applied less than a limit of 45° [9]. In addition, the shape of the projected section not only affects the failure load but also influences the vertical settlement of under-reamed piles [32].

PIV is a method for evaluating the velocity field(s) of fluids or particles using captured images with a digital camera or illumination [3, 4, 38, 43, 50]. Since its development, PIV has been applied in various fields, such as fluid mechanics [6, 52] and chemical engineering [37, 53]. There have been several attempts to quantitatively assess soil deformations or displacements by using PIV in geotechnical engineering since 2001, including GeoPIV, MatPIV, PIVlab, and PIVTEC [20, 56, 58, 63, 64]. Recently, there have been attempts to assess the behavior of the ground around an under-reamed pile using PIV. Harris and Madabhushi [23] analyzed ground behavior by the shape of the under-reamed angle when uplift loading occurred using PIV [23]. Qi et al. [47] used PIV to confirm the vertical and horizontal displacement of the soil due to the deformation of the expanded-base pile [47]. Particle image velocimetry (PIV) analysis has been attempted to investigate the failure mechanisms of sand due to the pull–out of an enlarged base pile under various ground conditions [51]. Ads et al. [5] used the PIV technique to examine the behavior of nature-based deep foundations in fused quartz and a mixture of mineral oils instead of soil [5].

In this way, much research has been conducted to increase load carrying capacity and reduce pile displacement by adding a reaming section (projected section) to the pile shaft. Various studies have been conducted on pile and soil behavior caused by the shape

of the projected section. However, because the self-weight of the soil affects the behavior of the ground, it is difficult to fully investigate the effect of the projected section on penetration resistance and soil behavior. In situations where self-weight is not considered, no research has been conducted on the effect of the projected section on the ground. Therefore, the present study investigated the effects of the projected section shape variation on the load–displacement and failure mechanism of surface-projected piles via two-dimensional small-scale model test and PIV analysis. The effect of the surface-projected section on penetration resistance at failure and failure mechanism of ground was experimentally assessed. The optimal condition shape of the surface-projected pile was presented using the results of this experiment.

Numerous studies have investigated enhancing load carrying capacity and minimizing pile displacement through the addition of a reaming section (projected section) to the pile shaft [1, 11, 13, 31, 33, 49]. However, research has yet to fully explore the effect of the only projected section on penetration resistance and ground behavior under surface-projected conditions. Therefore, this study aims to investigate the effects of the projected section shape variation on the surface-projected pile behavior. Through two-dimensional small-scale model tests and PIV analysis, the influence of the projected section on penetration resistance at failure and ground failure mechanisms is assessed. By incorporating both experimental and analytical approaches, this study seeks to bridge the gap between empirical observations and theoretical predictions, offering a more comprehensive understanding of pile behavior. The paper also compares experimentally determined penetration resistances and theoretically determined bearing capacities and presents various attempts to close this gap. In particular, the investigation focuses on how different projection dimensions and angles can be leveraged to enhance load capacity, providing critical insights for engineering design applications. The experimental findings contribute to confirming the increase in load carrying capacity resulting from surface-projected conditions and help identify the optimal shape for surface-projected piles.

Materials and methods

Experimental programs

A two-dimensional soil box made of transparent acrylic was used to investigate the penetration resistance of the surface-projected pile. Generally, model pile testing is most often performed in a three-dimension state and vertical penetration process. The advantage of performing a three-dimensional model test of pile is that the shape of the pile can be used as is. However, in this study, a model test was performed by laying down the soil box in a two-dimensional state to analyze the ground behavior induced by pile penetration through Particle Image Velocimetry (PIV) analysis. The two-dimensional model pile test in horizontal penetration system has the advantage of being able to determine the net bearing capacity enhancement effect increased by the projected section. For this reason, the two-dimensional model test procedure was used for the purpose of the research. This transparent soil box allows researchers to check ground behavior during experiments. The dimensions of the soil box were 900 mm (length) × 700 mm (width) × 300 mm (height). The surface-projected pile had dimensions of 1800 mm (length) × 100 mm (width) × 300 mm (height). Surface-projected acrylics were attached

on both sides of the model pile to implement the projected section of the surface-projected pile. A wire mesh was attached to the outermost inside the soil box to define the frictional boundary condition. To mobilize the friction between the pile surface and surrounding soils, sandpaper was attached along the surface of the model pile and the sides of projected sections.

The projected section is made of transparent acrylic with a stepped shape rather than a continuous trapezoid. The ideal projected section would be a continuous trapezoidal shape, which is often used in practice. However, in the model test, it was difficult to make the acrylic at the correct angle, so it was made by attaching several square sections of acrylic. Different surface-projected conditions (widths and angles) were considered summarized in Fig. 1. As shown in Fig. 1a, l denotes the length of the projected section, w_m denotes the width of the model pile, w_p denotes the projected width, and θ denotes the projected angle. The projected widths (w_p) were 10 mm, 20 mm, and 40 mm, where different projection angles (θ) were additionally considered for w_p of 20 mm and 40 mm. Each plane area of the projected section was set as the same to only consider the projected angle change. When the w_p were 20 mm and 40 mm, the plane areas were 2000 mm^2 and 4000 mm^2, respectively. When $w_p = 20$ mm, the tested θ were 90°, 45°, 27°, and 18°, while for $w_p = 40$ mm, the $\theta = 90°$, 45°, and 27° were considered. For the test case symbols, "**W**" indicates the projected width, and "**AN**" denotes the projected angle. The summarized test variables are shown in Table 1 and Fig. 2b–i.

The resistance force and displacement occurring during the penetration of the surface-projected piles were measured using various measurement devices. The surface-projected pile was moved at a constant displacement rate using a gearbox. The load was

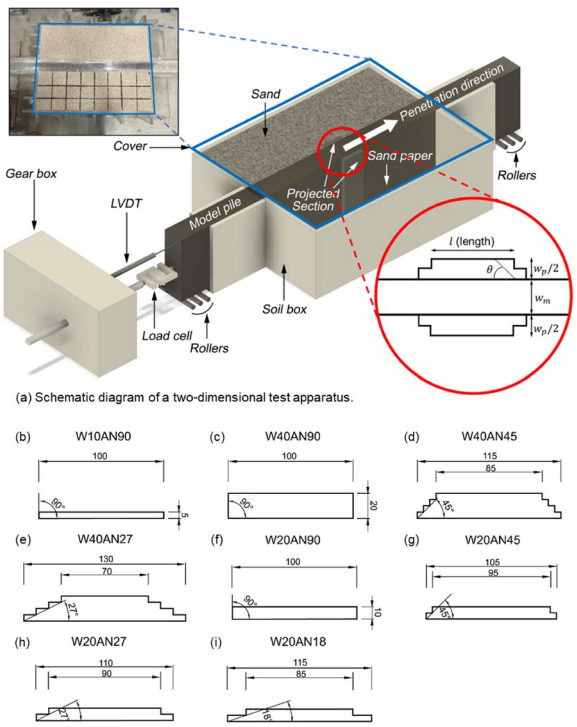

Fig. 1 Soil properties used in model test

Table 1 Model test variables

Test cases	Projected width (w_p) (mm)	Projected area (mm^2)	Projected angle (θ) (°)
NR	–	–	–
W10AN90	10	1000	90
W20AN90	20	2000	90
W20AN45			45
W20AN27			27
W20AN18			18
W40AN90	40	4000	90
W40AN45			45
W40AN27			27

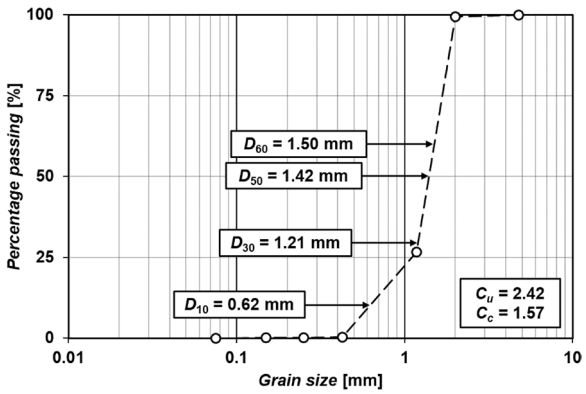

Fig. 2 Detailed views of penetration tests: **a** Schematic diagram of a two-dimensional test apparatus, **b**–**i** Variables of model tests

measured by connecting a load transducer between the gearbox and the model pile. The load transducer had a capacity of 50 kN. The penetration displacement of the model pile was measured using a 100-mm linear variable differential transformer (LVDT). A data logger and switch box were used to read and collect the measured data from the load transducer and LVDT.

The projected sections were fabricated by attaching acrylic protrusions on both sides of the model pile. The model pile (with the sandpaper and projected section) was placed in the center of the soil box (Fig. 1a). To eliminate friction with the floor caused by its own weight, rollers were placed at the bottom of the model pile. Bentonite-oil mixture was placed between the acrylic soil box and pile shaft prior to soil composition to prevent soil particles inflow. Bentonite reduces frictional resistance as a drilling fluid when combined with polymers [54], and oil-based bentonite has a high lubricating ability [10]. With these properties of oil-based bentonite, bentonite-oil mixture not only prevents soil particle inflow, but also minimizes the frictional resistance between the pile shaft and soil box. Sand was poured into the soil box using a sand pluviator to fill the spaces between the model pile and box walls. To form a uniform ground with a constant density, the sand was poured from a constant height. To assure the constant density of soil, three soil can samplers (50 mm diameter and 35 mm height) were placed near the edge

of soil box to avoid interference effects induced by surface-projected section. Each sampler was installed at different heights and locations. After the model tests, soil can samplers were carefully removed, and the weight of the soil in the samplers was measured to be 110 g, 109 g, and 110 g, respectively. This confirmed that the dry unit weight was 16 kN/m^3 at all heights. The model ground was uniformly sprayed at a height of 600 mm with three iterations of 100 mm each. After the model ground was formed, dyed (i.e., black) chalk was sprayed to effectively assess the soil particle displacement induced by the pile displacement of the model pile. The spacing of the dyed chalk was uniformly spread at 50 mm. To evaluate the ground behavior around the projected section of the model pile in detail, the spacing of dyed chalk was sprayed more closely at 25 mm around the projected section. A cover was placed and connected to the soil box to prevent the ground from rising when penetrating the model pile. The penetration speed was constant at 1 mm/min. The shear rate in model test was set to be the same as that in the direct shear test in order to similarly simulate the shear behavior of soil. The model pile was penetrated by a total displacement of 40 mm. For the particle image velocimetry (PIV) analysis, photographs were captured at the same position, brightness, and angle on the top of the soil box. Specifically, photographs were taken every time the pile displacement on the top of the soil box reached 1 mm.

Sand

In this study, dry "Jumunjin" natural sand from South Korea was used. The dry unit weight of soil was 16.0 kN/m^3. The maximum and minimum dry unit weights of the cohesionless soil [17] were determined as 17.9 and 14.6 kN/m^3, respectively. The relative density was 47%, corresponding to medium sand. The particle size distribution of the sand was determined using a sieve analysis test (Fig. 2). The coefficients of uniformity and curvature (C_u and C_c) were calculated as 2.42 and 1.57, respectively. According to the unified soil classification system [18], the sand used in this study was classified as "SP".

The mechanical properties were used to determine the shear strength of the soil. There are several methods to express the failure criterion of a soil. Especially, the Mohr–Coulomb failure criterion is widely used to express the relation between the shear stress (τ') and its normal stress (σ'). The shear parameters of the soil have the effective cohesion (c') and the effective internal friction angle (ϕ'). These shear parameters of the soil can be determined using a direct shear test [7]. According to ASTM D3080 [7], the shearing device should be able to apply the shear rate from 0.0025 to 1.0 mm/min. In this study, the shear rate at which peak stress occurs was determined through preliminary tests, and this shear rate is 1.0 mm/min. The direct shear test results are shown in Table 2. The effective cohesion is 0, and the effective internal friction angle is 37°.

Table 2 Physical and mechanical properties of sand

Physical properties				Mechanical properties	
USCS	**Dry unit weight, γ_d**	**Relative density, D_r**	**Mean diameter, D_{50}**	**Internal friction angle, φ**	**Cohesion, c**
SP	16.0 kN/m^3	47%	1.42 mm	37°	0 kPa

Particle image velocimetry (PIV) analysis

In this study, GeoPIV-reliability-guided (RG) software based on a MATLAB program command was used to indicate the displacement and maximum total shear strain of soil particle during the penetration of the surface-projected pile. The GeoPIV-RG is an updated version of GeoPIV which combines Leapfrog, sequential schemes and a reliability-guided scheme without trial-and-error [55]. Digital images were taken every 1 mm of pile displacement from the plan view of the soil box while maintaining a constant brightness during surface-projected pile movement, where 40 images were captured at the same location during the penetration test. The correlation between the failure displacement of the ground (as determined through the load–displacement curve) and PIV analysis results can be confirmed by applying PIV analysis. In addition, the influence zone and failure mechanism of the ground can be determined using the correlation between the particle displacement and maximum total shear strain at the ground failure points.

Experimental results of penetration resistance

Failure points of ground induced by pile displacement

The load–displacement relation of pile penetration is nonlinear when the local or punching shear failure of foundation occurs. This relation makes it difficult to judge the failure point of adjacent ground. To judge the failure point, Mansur and Kaufman [42] proposed to define the intersection point between the initial and final tangent lines of the load–displacement curve as the ultimate bearing capacity of pile [42]. Vesić [60] suggested the point having the steepest tangential line along the load-settlement curve to be regarded as the load at failure [60]. Hirany and Kulhawy evaluated the mechanical behavior of piles using two points in the load–displacement curve of a pile where linear lines occur [24–26]. This method is known as the $L_1 - L_2$ method. Among different methods mentioned above, the tangent intersection method has mainly been used for various pile types including helical piles and micro piles [2, 12, 28, 59]. In this study, the penetration resistance at failure ($\boldsymbol{P_f}$) and the pile displacement ($\boldsymbol{\delta_p}$) at failure ($\boldsymbol{\delta_{p,f}}$) of surface-projected piles were determined following the tangent intersection method.

Projected width effect on the penetration resistance for projected angle ($\theta = 90°$)

The load–displacement curves of surface-projected piles with different projected width and angle cases are plotted in Fig. 3. The pile with no surface projection (NR) has shown that linear penetration resistance increases up to 2 mm of displacement, then shows non-linear behavior whilst becoming linear beyond 10 mm of displacement (Fig. 3a). The penetration resistance at failure ($\boldsymbol{P_f}$) of the ground for plain pile (NR) has been assessed as 1.17 kN at 4.63 mm of displacement by the tangent intersection method [26].

As shown in Fig. 3a–d, the load–displacement curves of model piles with $\boldsymbol{\theta} = 90°$ showed linear ($\boldsymbol{\delta_{p,f}} < 1$ mm and $\boldsymbol{\delta_{p,f}} \geq 10$ mm) and nonlinear ($1\ \text{mm} \leq \boldsymbol{\delta_{p,f}} < 10$ mm) paths, where the slope at initial state is greater than that at residual state (Fig. 3a–d).

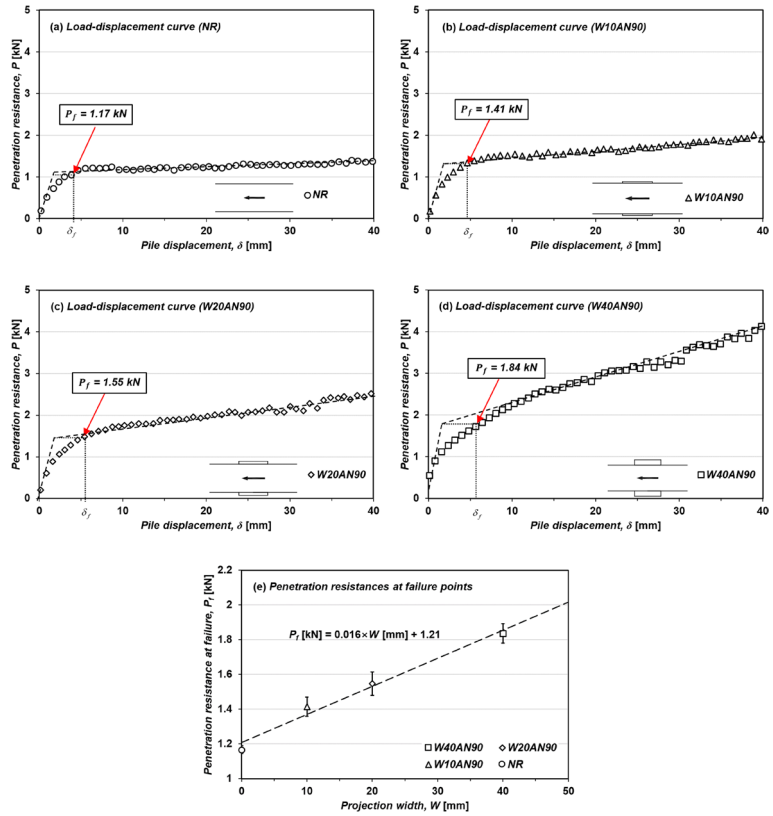

Fig. 3 Penetration results of surface-projected piles with the perpendicular (90°) projected angle and different projected widths

The penetration resistances at failure (P_f) for w_p = 10 mm, 20 mm, and 40 mm were 1.41 kN, 1.55 kN, and 1.84 kN, respectively. The pile displacement at failure ($\delta_{p,f}$) increased as w_p increased, as 5.74 mm (w_p = 10 mm), 6.25 mm (w_p = 20 mm), and 6.45 mm (w_p = 40 mm). Figure 3e summarizes P_f with w_p for θ = 90°, where P shows a linear increase with w_p.

Projected angle effect on the penetration resistance

Projected width of w_p = 20 mm

The results from penetration tests on piles with the same projected width (w_p = 20 mm) and different θ are shown in Fig. 4. The P_f values were 1.55 kN, 1.67 kN, 1.75 kN, and 1.72 kN for θ = 90°, 45°, 27°, and 18°, respectively (Fig. 4a–d). The load–displacement curves for surface-projected piles with w_p of 20 mm showed that P_f is largest for θ = 27°, and smallest for θ = 90°. As summarized in Fig. 4e, P_f gradually decreases with the increase of θ.

Projected width of w_p = 40 mm

Figure 5 shows the penetration test results of w_p = 40 mm model piles with different θ. The P_f values were assessed as 1.84 kN, 1.80 kN, and 1.77 kN for θ of 90°, 45°, and 27°, respectively, from each load–displacement curve (Fig. 5a, b and c). The P_f of w_p = 40 mm model piles gradually increases with higher θ (Fig. 5d), which is contrary to the P_f trend

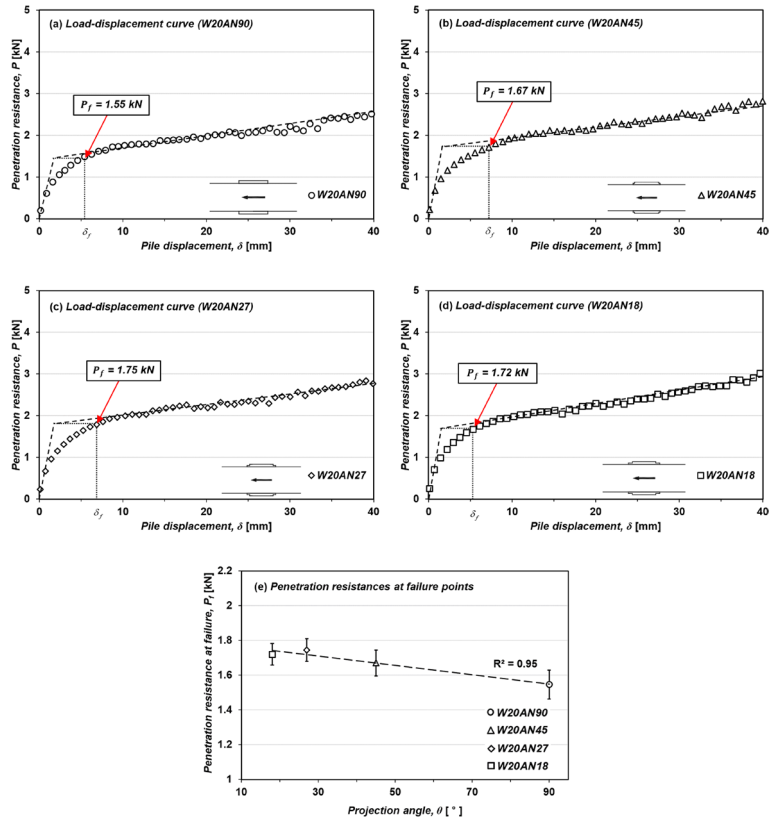

Fig. 4 Penetration results of surface-projected piles with the same projected width (20 mm) and different projected angles

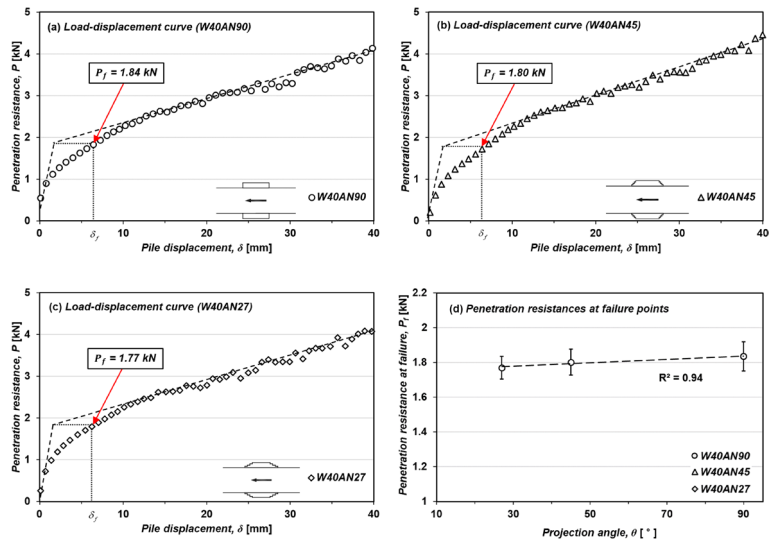

Fig. 5 Penetration results of surface-projected piles with the same projected width (40 mm) and different projected angles

Table 3 Model test results

Test cases	Displacement at failure, $\delta_{p,f}$ (mm)	Penetration resistance at failure, P_f (kN)
NR	4.63	1.17
W10AN90	5.74	1.41
W20AN90	6.25	1.55
W20AN45	6.67	1.67
W20AN27	6.06	1.75
W20AN18	5.85	1.72
W40AN90	6.45	1.84
W40AN45	6.90	1.80
W40AN27	6.01	1.77

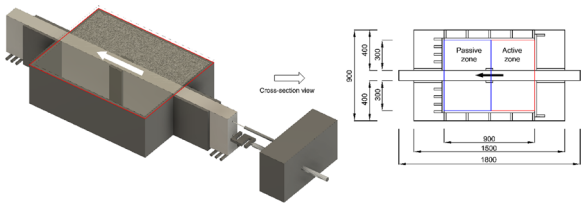

Fig. 6 Cross-sectional view of passive and active zone induced by projected section

of $w_p = 20$ mm (Fig. 4e) model piles. Table 3 summarizes the $\delta_{p,f}$ and corresponding P_f values for all test cases conducted in this study.

Ground behavior analysis through PIV

The ground behavior and plastic failure during pile displacement were investigated through PIV analysis. The ground behaviors and particle displacements were assessed for cases with θ of 90° and different w_p (NR, W10AN90, W20AN90, and W40AN90). Cross-sectional view of the soil box is shown in Fig. 6. When a model pile is moved, a passive zone (blue box), which is compressed by the projected section, and an active zone (red box), which is tensional, are generated. To assess the particle displacement generated by the projected section, PIV analysis was performed only on the soil in the passive zone. The PIV analysis results are shown in Fig. 7a–d. Figure 7 shows a zoomed-in view of the passive zone when displacement of surface-projected piles occurs. The upper and lower parts of Fig. 7 are symmetric conditions and are all the same soil in one figure. However, the upper parts of the figures show the shading of the particle displacement, and the contours and vectors of the particle displacement are shown in the lower parts. As shown in Fig. 7a–d, δ_p is the pile displacement and $\delta_{p,f}$ is the pile displacement at failure.

The PIV analysis results show that the particle displacement increases as the δ_p increases in all four cases. When the pile movement occurs, the particle moves in the same direction as the pile movement. This is because the arching effect occur in soil during pile movement [19, 30]. Particle displacement occurs until ground failure in all four cases when the piles move. In the case of NR (Fig. 7a) and W10AN90 (Fig. 7b), the particle displacement no longer occurred after the ground failed due to pile displacement.

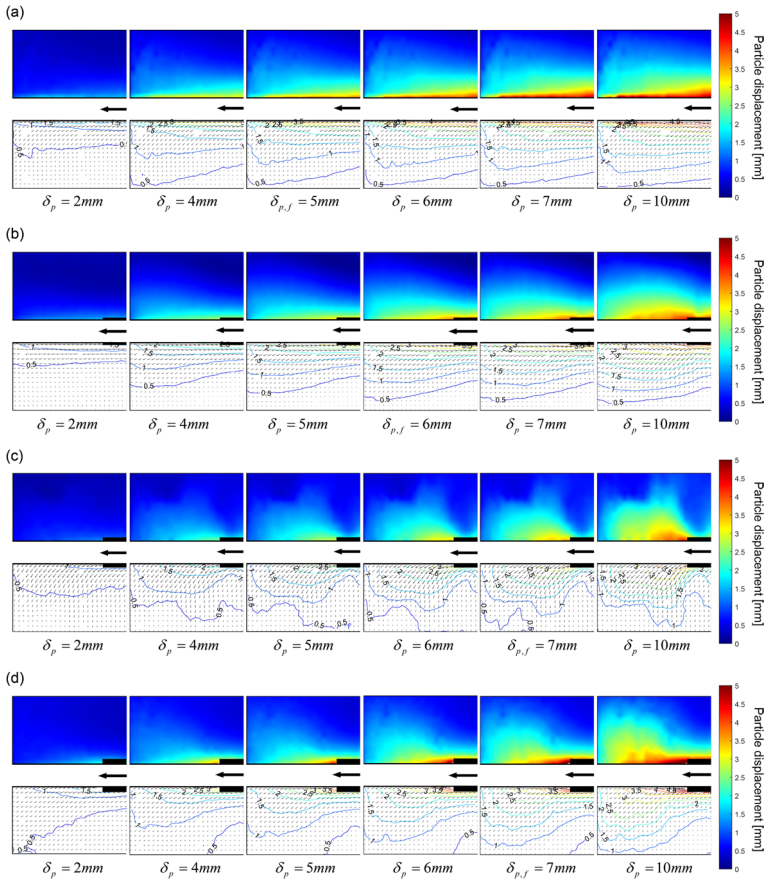

Fig. 7 Ground behaviors induced by pile displacements with different projected widths: **a** NR, **b** W10AN90, **c** W20AN90, **d** W40AN90

However, in the cases of W20AN90 (Fig. 7c) and W40AN90 (Fig. 7d), the particle moves continuously even though the surface-projected pile moves after failure. This means that when the w_p is small, a residual P_f cannot be expected after ground failure. The ground around the projected section undergoes plastic failure and does not generate a shear resistance. When the w_p is large, a residual resistance can be expected after ground failure, and it has been shown that an additional passive resistance is generated by the projected section.

Discussions

Bearing capacity of surface-projected piles

The penetration resistance at failure of surface-projected pile was determined by model test. In addition, the bearing capacity of the surface-projected pile can be calculated by the theoretical formula (Q_u). In this chapter, experimental P_f and theoretical Q_u were compared for piles with θ of 90°. There are various methods for determining the bearing capacity of a pile proposed by various researchers. However, all these formulas consider the self-weight of the soil. The soil box and model pile used in this study are designed to minimize the soil's self-weight. Therefore, a different formula should be applied to determine the effect of increasing the bearing capacity by the surface-projected part.

Theoretical $\boldsymbol{Q_u}$ of surface-projected pile was determined using the theoretical formula of Prandtl [45]. Prandtl assumed that the soil was weightless, and Prandtl used Kötter's equation [34] to calculate the failure mechanism of the soil [45, 46]. Prandtl applied this assumption to the symmetric slope under stresses (i.e., major and minor principal stress). These stresses were applied to a slope where the major principal stress direction was vertical and symmetrical about the vertical central axis. The distributed vertical load (i.e., major principal stress) acted on the slope's upper part. The distributed normal load (i.e., minor principal stress) acted on the edge planes of the slope. By changing the angle of the symmetrical slope by 180°, the bearing capacity formula caused by pile penetration can be obtained. In addition, considering dried sandy soil ($\boldsymbol{\gamma}=0$, $\boldsymbol{c}=0$, $\boldsymbol{\phi}\neq 0$), the model test setup corresponds to a Prandtl material. Therefore, the theoretical formula for obtaining Prandtl's pile bearing capacity can be used. The bearing capacity formula (i.e. major principal stress, p_1) of the pile is given by Eq. (1).

$$p_1 = p_3 \tan^2(\pi/4 + \phi/2)e^{2\pi \tan\phi} \tag{1}$$

In Eq. (1), the minor principal stress (p_3) can be calculated by using the earth pressure at rest. The coefficient of the earth pressure at rest can be calculated using Jaky's equation [30]. The minor principal stress is given by Eq. (2).

$$p_3 = \frac{1}{2}K_0\gamma_d h_s = \frac{1}{2}(1-\sin\phi)\gamma_d h_s \tag{2}$$

where, K_0 is the coefficient of the earth pressure at rest, γ_d is the dry unit weight of the soil, and h_s is the height of the soil box.

When the soil properties (Fig. 2) are substituted into Eq. (2), the minor principal stress is 0.96 kN/m^2. Moreover, by substituting the minor principal stress (p_3) into Eq. (1), the major principal stress (p_1) can be calculated, and this value is 437.61 kN/m^2. The tip bearing capacity and skin friction can be calculated by multiplying the major principal stress by the area of the tip and skin area, respectively. The total $\boldsymbol{Q_u}$ of the surface-projected pile adds to the tip bearing capacity and skin friction. The area of the tip is obtained by multiplying the height and width of the projected section. The skin area is determined by multiplying the height of the projected section by the length of the pile excluding the plastic zone. Since the length of the plastic zone depends on the projected width, the area of skin decreases as the projected width increases. The length of the model pile does not affect the shear resistance of the

Table 4 Theoretical bearing capacities and experimental penetration resistances at each case

Test cases	Point area (m^2)	Skin area (m^2)	Tip bearing capacity (kN)	Skin friction (kN)	Theoretical bearing capacity, Q_u (kN)	Modified theoretical bearing capacity, $Q_{u,m}$ (kN)	Experimental penetration resistance at failure, P_f (kN)
NR	–	0.270	–	0.39	0.39	0.35	1.17
W10AN90	0.003	0.243	1.31	0.35	1.66	0.49	1.41
W20AN90	0.006	0.219	2.63	0.31	2.93	0.65	1.55
W40AN90	0.012	0.165	5.25	0.23	5.49	0.94	1.84

plastic failure body. Therefore, the pile length is calculated by subtracting the height of the plastic body from the total pile length. The calculated Q_u is shown in Table 4.

The theoretical Q_u and experimental P_f increase as the w_p increases (Table 4). Furthermore, as the theoretical Q_u increases, so does the difference between the theoretical Q_u and experimental P_f. The reason for this variation is due to the difference in failure types. The Q_u through Prandtl's formula is calculated by assuming that a general shear failure occurs in the ground as a result of the pile penetration. The experimental P_f of model pile in sand was less than estimated by the theoretical Q_u because the compressibility effect of soil was neglected in Prandtl's theory [48]. The assumed failure surface does not occur in loose and medium dense soil. Theoretical bearing capacity factors can be applied only to dense soil where general shear failure occurs. Furthermore, the load–displacement curve has the peak load when the general shear failure occurs in the ground. However, as shown in Figs. 3, 4, 5, the load–displacement curves do not have peak loads, but rather have gradually increased loads as the displacement increases. This means that the general shear failure did not occur, and that a local shear failure occurred. When a local shear failure occurs, the shear parameters (cohesion parameter c and friction parameter tan ϕ) are multiplied by two-thirds to calculate the bearing capacity [57]. As a result of recalculation by multiplying the shear parameters by 2/3, the experimental P_f by increasing w_p was larger than the modified theoretical Q_u ($Q_{u,\,m}$) (Fig. 8). The increments of bearing capacity occurred similarly for P_f and $Q_{u,\,m}$ as w_p increased. Only the y-axis intercept, that is P_f and $Q_{u,\,m}$ in the NR case with $w_p = 0$ mm, were different, which is the difference in skin friction applied to the model pile. The reason for this difference is the frictional relation between pile and soil in zone III in Prandtl-wedge. Prandtl presented the Prandtl-wedge failure mechanism, and Prandtl wedges were divided the failure mechanism of soil into zone I, II, and III [45]. In the case of Prandtl-wedge's zone III, it is assumed that there is no friction at all on the surface of the ground. Since this concept was taken to the failure mechanism of piles, no surface frictional resistance between soil and piles in zone III was assumed. Accordingly, the bearing capacity using Prandtl's theoretical formula calculates only the friction caused by horizontal stress (i.e., the major principal stress) without shaft friction. On the other hand, in the experimental P_f, not only the friction due to the confinement but also the friction acting on the pile

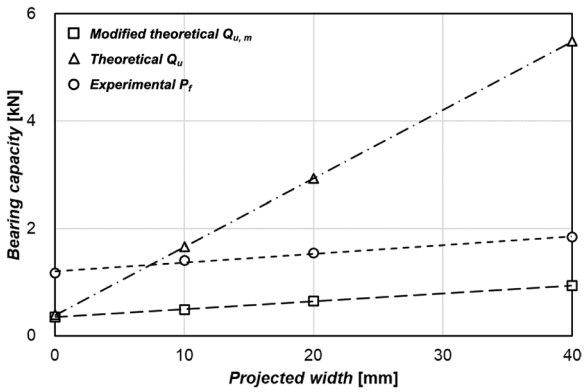

Fig. 8 Comparison of increasing trend between P_f, Q_u, and $Q_{u,\,m}$ as w_p increase

shaft worked together. Therefore, the experimental P_f occurred larger than the theoretical $Q_{u,m}$.

The values of modified theoretical $Q_{u,m}$ and experimental P_f occurred differently. On the other hand, the tendency of bearing capacity to increase as w_p increased was the same. This indicates that the ultimate bearing capacity formula by Prandtl can be used to predict the load improvement effect due to increased projected width. The results of this study can be used to predict the increase trend compared to shaft piles when designing surface-projected piles in medium sand. However, it is determined that verification via numerical modeling or model testing is required in order to accurately assess ultimate bearing capacity. As shown in Fig. 1, the theoretical Q_u of piles with the same w_p and different θ should be the same because the plan area of the surface-projected section was same. This is because the area of the tip and skin does not change even if the θ is changed. However, as shown in Figs. 4e and 5d, when the θ is changed, the P_f differs. In the case of a w_p of 20 mm, the smaller the θ, the larger the P_f. In the case of a w_p of 40 mm, the P_f is proportional to the θ. This demonstrates that when the w_p is small, the effect of the additional skin area as the θ increases outweighs the effect of the tip bearing capacity of the projected section. When the w_p is large, the effect of the tip bearing capacity generated by the projected section is greater than the effect of the skin friction, and the larger the θ of the pile, the greater the P_f.

Failure mechanism induced by displacement of surface-projected pile

The failure mechanism was investigated by comparing the maximum total shear strain (γ_{max}) in the PIV analysis with the theoretical plastic failure size. Figures 9a and b show the theoretical plastic failure and γ_{max} of the piles with w_p of 20 mm and 40 mm, respectively. The theoretical failure mechanisms of the soil were calculated using the Prandtl's

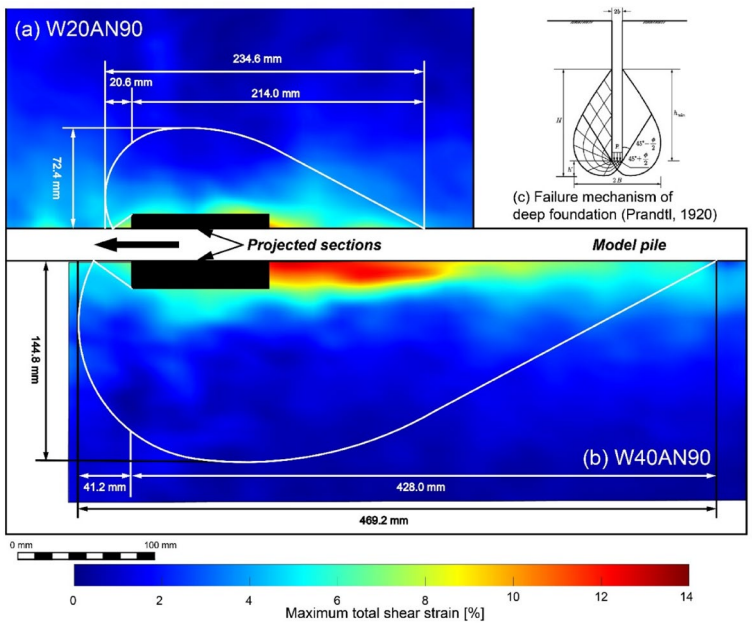

Fig. 9 Comparison between theoretical and experimental failure mechanism for projected width: **a** W20AN90, **b** W40AN90 and **c** Failure mechanism of deep foundation [45]

formula. If the slope angle is π, the ground behavior corresponds to the failure mechanism of a deep foundation, as shown in Fig. 9c. The bearing capacity equation of a deep foundation is expressed as shown in Eqs. (1) and (2). In addition, the magnitude of the plastic failure body around the deep foundation is expressed by Prandtl's formula. The failure mechanism and influence zone of the ground by pile penetration can be verified using Eq. (3).

$$\begin{aligned} H = h_{\min} + h' &= 2b\left[\tan\left(\frac{\pi}{4}+\frac{\phi}{2}\right)e^{\pi\tan\phi} + \frac{1}{2}\frac{\cos\phi}{\cos\left(\frac{\pi}{4}+\frac{\phi}{2}\right)}e^{\left(\frac{\pi}{4}+\frac{\phi}{2}\right)\tan\phi}\right] \\ 2B &= 2b\left[1+\frac{\cos\phi}{\cos\left(\frac{\pi}{4}+\frac{\phi}{2}\right)}e^{\left(\frac{3\pi}{4}+\frac{\phi}{2}\right)\tan\phi}\right] \end{aligned} \tag{3}$$

Here, $\boldsymbol{H}$ is the total height of the plastic failure, $\boldsymbol{h'}$ is the plastic failure height below the pile tip, $\boldsymbol{h_{min}}$ is the plastic failure height above the pile tip, $\boldsymbol{2B}$ is the width of the plastic failure, and $\boldsymbol{2b}$ is the pile width. As shown in Fig. 9a and b, the white lines and curves represent the theoretical plastic failure body. The heights of theoretical failure shape and $\boldsymbol{\gamma_{max}}$ are the same in both cases (W20AN90 and W40AN90). However, the width of the theoretical failure is wider than that of the experimental failure body. This is because the theoretical failure shape is calculated while assuming that the ground is subject to a general shear failure. In PIV analysis, Fig. 9a and b showed that local shear failure occurred in the soil due to the pile displacement because $\boldsymbol{2B}$ is relatively smaller than that of general shear failure body.

The differences in the penetration resistances at each failure induced by the change of the $\boldsymbol{\theta}$ were investigated using a PIV analysis. The $\boldsymbol{\gamma_{max}}$ was confirmed by zooming in the passive earth pressure zone (compressive zone) induced by the pile displacement. As shown in Fig. 10a and b ($\boldsymbol{w_p}$ = 20 mm), the contour of the $\boldsymbol{\gamma_{max}}$ in the case of W20AN18 is larger than that in the case of W20AN90. However, in Fig. 10c and d ($\boldsymbol{w_p}$ = 40 mm), a larger $\boldsymbol{\gamma_{max}}$ occurs when the $\boldsymbol{\theta}$ is 90° relative to when it is 27°. The $\boldsymbol{\gamma_{max}}$ with a greater width and length has a greater adhesion to the pile, resulting in a higher bearing capacity of the pile. The PIV results corresponded to the load–displacement curves (Figs. 4e and 5d). The effects of the $\boldsymbol{w_p}$ and $\boldsymbol{\theta}$ on $\boldsymbol{P_f}$ were quantitatively assessed using the PIV analysis, and the effectiveness of the PIV analysis was confirmed.

Optimal surface-projected condition for cost-effective construction

The $\boldsymbol{P_f}$ induced by the pile movement were proportional to the projected $\boldsymbol{w_p}$ (Fig. 3e). The $\boldsymbol{P_f}$ of the pile with $\boldsymbol{w_p}$ = 40 mm (W40AN90) increased by up to 57% compared to the control (NR). When compared to NR, a sufficient bearing capacity can be secured even for surface-projected piles of the same length or width. Alternatively, when designing a pile with the same bearing capacity, the width or length of the surface-projected pile can be reduced.

As a result of this study, the projected angle affects the pile's bearing capacity. In previous studies, the projected angle was set to 30–45° for economical construction [35], and the bell shape of the surface-projected pile was designed for a maximum

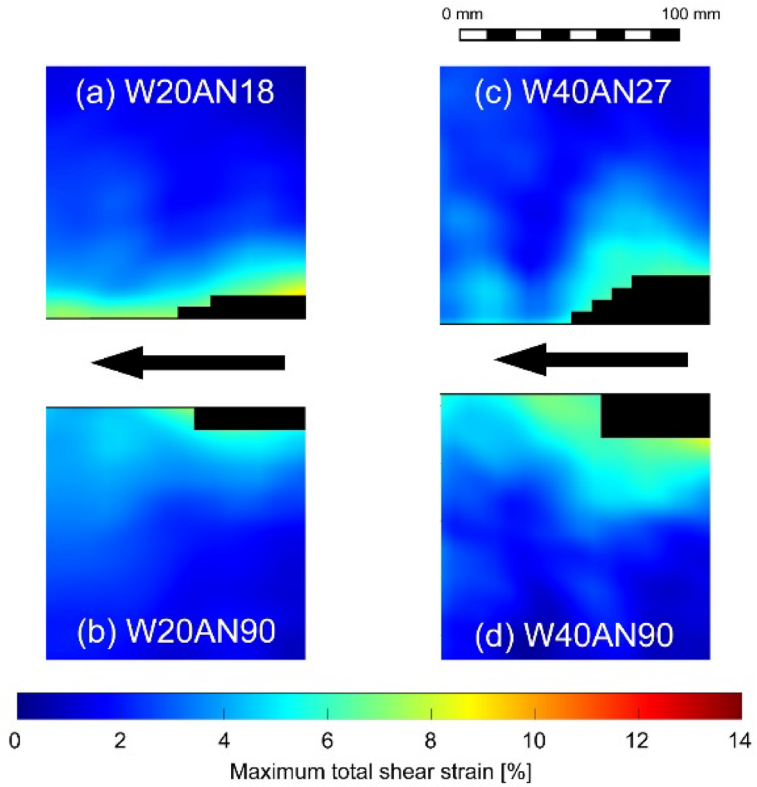

Fig. 10 Comparison of maximum total shear strain between each pile with different projected widths and angles

of 45° to prevent a punching shear failure [27]. Furthermore, owing to construction errors, it is difficult to implement a projected angle of 90°. The optimal projected condition resulting from the size of the w_p can be proposed using the results in this study. When the w_p is 20 mm and the θ are 18°–45°, reasonable P_f can be secured. This range is similar to the economical construction range of 30°–45°. In the case of a small w_p, it is ideal to design a small projected angle. When the θ are 27°–45° in a pile with a w_p of 40 mm, reasonable P_f can be secured. This indicates that when the w_p is 40 mm, it is advantageous to design a large θ, i.e., similar to the range applied when considering economic conditions. Furthermore, similar P_f are observed when the θ was 27° and the w_p are 20 mm and 40 mm, respectively. This means that, considering the workability and economic feasibility, when the θ is 27°, it is possible to secure a sufficient bearing capacity even if the w_p is designed smaller. However, because the projected widths and angles used in this paper are limited, the optimal surface-projected condition determined only applies to shaft-type surface-projected piles in medium sand. Additional research on more diverse soil types, D_{50}, relative density, widths and angles is needed to determine the most effective surface-projected condition. Also, the ground used in the model test is loose sand, which is different from the actual ground conditions in the field and may cause different ground behavior. The exact effect of the increase in bearing capacity by surface projection requires a penetration test of the pile in the field, and further research is needed.

Conclusions

The projected shape affects the penetration resistance of a pile. In particular, the w_p and θ are closely related to the bearing capacity of a surface-projected pile. In this study, the P_f induced by the δ_p were assessed through a two-dimensional model test. For the failure mechanism of the ground, photographs were taken, and a PIV analysis was performed. The following conclusions were obtained.

The P_f were proportional to the w_p of the pile when θ is 90°. When the w_p was 20 mm, the P_f and θ were inversely proportional. In the case of w_p = 40 mm, the P_f increased as the θ increased. The theoretical Q_u of the surface-projected pile could be calculated using Prandtl's theory. Through this theory, the enhancement effect of projected section on the Q_u was obtained. There were differences between the theoretical Q_u and the P_f determined through experiments, and these differences were the proportional to the projected width increase. To eliminate this difference, new $Q_{u,\,m}$ was calculated by multiplying the shear parameters (cohesion and internal friction angle) by 2/3. As a result of recalculation of modified theoretical ultimate bearing capacity $Q_{u,\,m}$ of pile, increment of load was the same, only difference in skin friction was found. This is because the shaft friction between soil and pile was not considered in Prandtl's theoretical calculation formula, so the experimental P_f was larger. Through these results, it was shown that the failure mechanism of piles in medium sand is the local shear failure.

The ground failure mechanism and particle displacement induced by pile movement were evaluated using a PIV analysis. When the pile moved, particle displacement occurred in the penetration direction. In the case of the NR and W10AN90, the particle no longer moved after the failure point. In the cases of the W20AN90 and W40AN90, particle displacement continued to occur even after the failure point. This means that a residual P_f can be expected when the w_p is 20 or 40 mm.

The theoretical failure pattern through Prandtl's theory and experimental failure mechanism were compared. The height of plastic zone was similar to that determined by theory and experiment. However, the width of the plastic zone was small in the experiment relative to that in theory. This means that a general shear failure did not occur in the ground due to the pile displacement. The γ_{max} induced by the change of the θ of a pile with the same w_p was assessed. In the case of w_p = 20 mm, the largest contour of shear strain occurred when the θ was 18°. In the case of w_p = 40 mm, the most widespread contour of the shear strain occurred when the θ was 90°. These results correspond to the experimental test results, and the results from the PIV analysis are considered as reasonable and effective.

The experimental results obtained by this model test may differ from the 3-dimensional pile penetration test with a circular cross-section due to different conditions and designs. Also, there are differences between vertical penetration tests and horizontal penetration tests. Failure patterns of ground derived by vertical penetration tests that simulate real field ground and horizontal penetration tests for model tests may occur differently due to the effects of gravity. However, this study does not simulate real scale, but rather focuses on the effect of surface projection on increasing the load carrying capacity of the pile. Therefore, further studies are needed to set up a 3-dimensional model test with practical ground conditions.

Abbreviations

w_m	The width of the pile shaft
w_p	The projected width of the model pile
θ	The projected angle of the model pile
P_f	The penetration resistance at failure
$\delta_{p,f}$	The pile displacement
δ_p	The pile displacement at failure
Q_u	The theoretical bearing capacity of pile
γ	The unit weight of the soil
c	The cohesion of the soil
φ	The friction angle of the soil
p_1	The major principal stress of the soil
p_3	The minor principal stress of the soil
K_0	The coefficient of the earth pressure at rest
γ_d	The dry unit weight of the soil
h_s	The height of the soil box
$Q_{u,m}$	The modified theoretical bearing capacity of pile

Acknowledgements
This work was supported by the National Research Foundation of Korea (NRF) grant funded by the Korea government (MSIT) (No. 2022R1A2C2091517).

Author contributions
S.P. and G.K. conducted experimental tests and data analysis. S.P. mainly prepared figures. S.P. and I.C. wrote the main manuscript text and all authors reviewed the manuscript.

Data availability
No datasets were generated or analysed during the current study.

Declarations

Competing interests
The authors declare no competing interests.

Received: 7 August 2024 Accepted: 2 October 2024
Published online: 07 November 2024

References

1. Abbas HO (2020) Laboratory evaluation of effective parameters on uplift force under reamed pile in expansive soil. Geotech Geol Eng 38(4):4243–4252. https://doi.org/10.1007/s10706-020-01292-8
2. Adams MT, Collin JG (1997) Large model spread footing load tests on geosynthetic reinforced soil foundations. J Geotech Geoenviron Eng 123(1):66–72. https://doi.org/10.1061/(ASCE)1090-0241(1997)123:1(66)
3. Adrian RJ (1984) Scattering particle characteristics and their effect on pulsed laser measurements of fluid flow: speckle velocimetry vs particle image velocimetry. Appl Opt 23(11):1690–1691. https://doi.org/10.1364/AO.23.001690
4. Adrian RJ (1991) Particle-imaging techniques for experimental fluid mechanics. Annu Rev Fluid Mech 23(1):261–304. https://doi.org/10.1146/annurev.fl.23.010191.001401
5. Ads A, Iskander M, Pipin G (2023) Lessons in geomechanics of deep foundations from nature. Acta Geotech. https://doi.org/10.1007/s11440-023-01960-y
6. Aroussi A, Grant I, Yan YY (1991) Forced convection in joined rectangular grooves numerical simulation of PIV and LDA measurements. ICIASF Record, International Congress on Instrumentation in Aerospace Simulation Facilities, 94–102. https://doi.org/10.1109/ICIASF.1991.186230
7. ASTM D3080/D3080 M-11 (2011) Standard test method for direct shear test of soils under consolidated drained conditions. ASTM D3080/D3080 M-11, ASTM International, West Conshohocken, PA, USA. https://doi.org/10.1520/D3080_D3080M-11
8. Basha AM, Eldisouky EA (2023) Effect of eccentric loads on the behavior of circular footing with/without skirts resting on sand soil. Int J Geo-Eng 14(1):13. https://doi.org/10.1186/s40703-023-00192-z
9. Bowles JE (1996) Foundation analysis and design. McGraw-Hill, New York
10. Buyanovskii IA, Tatur IR, Samusenko VD, Solenov VS (2020) Effect of antifriction solid additives on the temperature stability of bentonite greases. J Frict Wear 41(6):492–496. https://doi.org/10.3103/S1068366620060057
11. Collins LE (1953) A preliminary theory for the design of underreamed piles. Civil Engineering = Siviele Ingenieurswese 1953(11)
12. Consoli NC, Schnaid F, Milititsky J (1998) Interpretation of plate load tests on residual soil site. J Geotechn Geoenviron Eng 124(9):857–867. https://doi.org/10.1061/(ASCE)1090-0241(1998)124:9(857)
13. Cooke RW, Whitaker T (1961) Experiments on model piles with enlarged bases. Géotechnique 11(1):1–13. https://doi.org/10.1680/geot.1961.11.1.1
14. Das BM (2010) Principles of Foundation Engineering. Cengage Learning, Boston

15. Dickin EA, Leung CF (1990) Performance of piles with enlarged bases subject to uplift forces. Can Geotech J 27(5):546–556. https://doi.org/10.1139/t90-070
16. Dickin EA, Leung CF (1992) The influence of foundation geometry on the uplift behaviour of piles with enlarged bases. Can Geotech J 29(3):498–505. https://doi.org/10.1139/t92-054
17. DIN 18126 (1996) Soil investigation and testing - Determination of density of non-cohesive soils for maximum and minimum compactness. DIN 18126, Beuth publishing DIN, Germany. https://doi.org/10.31030/7209583
18. DIN 18196 (2011) Earthworks and foundations - Soil classification for civil engineering purposes. DIN 18196, Beuth publishing DIN, Germany. https://doi.org/10.31030/1754896
19. Franke E (1982) EA-Pfähle (Vol. 3 Aufl). Ernst & Sohn, Germany
20. GmbH P (2014) PIVview user manual. P. GmbH, http://www.pivtec.com
21. Gomaa AE, Hasan AMM, Mater YM, AbdelSalam SS (2023) Shell folded footings using different angles and EPS cavity filling: experimental study. Int J Geo-Eng 14(1):10. https://doi.org/10.1186/s40703-023-00187-w
22. Hao D, Chen R, Fan G (2012) Ultimate uplift capacity of transmission tower foundation in undisturbed excavated soil. Energy Procedia 17:1209–1216. https://doi.org/10.1016/j.egypro.2012.02.228
23. Harris DE, Madabhushi GSP (2015) Uplift capacity of an under-reamed pile foundation. Proc Inst Civil Eng Geotech Eng 168(6):526–538. https://doi.org/10.1680/jgeen.14.00154
24. Hirany A, Kulhawy F (1988) Conduct and interpretation of load tests on drilled shaft foundations: Volume 1 detailed guidelines.
25. Hirany A, Kulhawy FH (1989) Interpretation of load tests on drilled shafts—Part 1: Axial compression. Foundation engineering: Current principles and practices, ASCE, 1132–1149.
26. Hirany A, Kulhawy FH (2002) On the interpretation of drilled foundation load test results. Deep Foundations 2002: An International Perspective on Theory, Design, Construction, and Performance: 1018–1028. https://doi.org/10.1061/40601(256)71
27. Honda T, Hirai Y, Sato E (2011) Uplift capacity of belled and multi-belled piles in dense sand. Soils Found 51(3):483–496. https://doi.org/10.3208/sandf.51.483
28. Housel WS (1966) Pile load capacity: estimates and test results. J Soil Mech Found. https://doi.org/10.1061/JSFEAQ.0000887
29. Iyer T, Rao N (1970). Model studies on funicular shells as rafts on sands. Proceedings, Symposium on Shallow Foundations, Bombay, India,
30. Jaky J (1944) The coefficient of earth pressure at rest. J Soc Hungarian Arch Eng. 355–358.
31. Jang Y-E, Han J-T (2017) Field study on axial bearing capacity and load transfer characteristic of waveform micropile. Can Geotech J 55(5):653–665. https://doi.org/10.1139/cgj-2017-0155
32. Jebur MM, Ahmed MD, Karkush MO (2020) Numerical analysis of under-reamed pile subjected to dynamic loading in sandy soil. IOP Confer Series: Mater Sci Eng 671(1):012084. https://doi.org/10.1088/1757-899x/671/1/012084
33. Khatri VN, Kumar A, Gupta SK, Dutta RK, Gnanandarao T (2019) Numerical study on the uplift capacity of under-reamed piles in clay with linearly increasing cohesion. Int J Geotech Eng. https://doi.org/10.1080/19386362.2019.1660527
34. Kötter F (1903) Die bestimmung des druckes an gekrümmten gleitflächen, eine aufgabe aus der lehre vom erddruck. Sitzungsberichte der Preussischen Akademie der Wissenschaften zu Berlin: 229–233.
35. Kumar A, Khatri VN, Gupta SK (2020) Effect of linearly increasing cohesion on the compression and uplift capacity of the under-reamed pile in clay. SN Appl Sci 2(2):315. https://doi.org/10.1007/s42452-020-2111-y
36. Li C, Ma X, Xue S, Chen H, Qin P, Li G (2021) Compressive capacity of vortex-compression nodular piles. Adv Civil Eng 2021:6674239. https://doi.org/10.1155/2021/6674239
37. Liu Z, Zheng Y, Jia L, Jiao J, Zhang Q (2006) Stereoscopic PIV studies on the swirling flow structure in a gas cyclone. Chem Eng Sci 61(13):4252–4261. https://doi.org/10.1016/j.ces.2006.01.024
38. Lourenco LM, Krothapalli A, Smith CA (1989) Particle image velocimetry. Springer, Berlin Heidelberg
39. Majumder M, Chakraborty D (2021) Effects of scour-hole dimensions and bulb positions on the lateral response of under-reamed pile in soft clay. Appl Ocean Res 117:102942. https://doi.org/10.1016/j.apor.2021.102942
40. Majumder M, Chakraborty D (2021) Three-dimensional numerical analysis of under-reamed pile in clay under lateral loading. Innov Infrastruct Solut 6(2):55. https://doi.org/10.1007/s41062-020-00428-2
41. Majumder M, Chakraborty D (2021) Uplift capacity and failure mechanism of under-reamed piles in clay based on lower bound finite element limit analysis. Proc Natl Acad Sci India Section A Phys Sci. https://doi.org/10.1007/s40010-021-00736-x
42. Mansur CI, Kaufman RI (1956) Pile tests, low-sill structures, old river, louisiana. J Soil Mech Found Div 82(4):715. https://doi.org/10.1061/TACEAT.0007594
43. Melling A (1997) Tracer particles and seeding for particle image velocimetry. Meas Sci Technol 8(12):1406–1416. https://doi.org/10.1088/0957-0233/8/12/005
44. Meyerhof GG (1976) Bearing capacity and settlement of pile foundations. J Geotech Eng Div 102(3):197–228. https://doi.org/10.1061/AJGEB6.0000243
45. Prandtl L (1920) Über die härte plastischer körper. Nachrichten von der Gesellschaft der Wissenschaften zu Göttingen Mathematisch-Physikalische Klasse 1920: 74–85. http://eudml.org/doc/59075
46. Prandtl L (1921) Hauptaufsätze: Über die eindringungsfestigkeit (härte) plastischer baustoffe und die festigkeit von schneiden. J Appl Math Mech 1(1):15–20. https://doi.org/10.1002/zamm.19210010102
47. Qi C-G, Zheng J-H, Zuo D-J, Chen G (2017) Measurement on soil deformation caused by expanded-base pile in transparent soil using particle image velocimetry (PIV). J Mt Sci 14(8):1655–1665. https://doi.org/10.1007/s11629-016-4025-0
48. Rogers FW (1962) Model studies of the point bearing capacity of foundations in a cohesionless soil Georgia Institute of Technology. Georgia, U.S.
49. Sakr M, Nasr A, Basha A, Khaffaf M (2023) Experimental and analytical assessment of the pullout capacity of axially loaded under-reamed pile in cohesionless soil. Innov Infrastruct Solut 8(1):73. https://doi.org/10.1007/s41062-023-01046-4

50. Santiago JG, Wereley ST, Meinhart CD, Beebe DJ, Adrian RJ (1998) A particle image velocimetry system for microfluidics. Exp Fluids 25(4):316–319. https://doi.org/10.1007/s003480050235
51. Schafer M, Madabhushi SPG (2020) Uplift resistance of enlarged base pile foundations. Indian Geotech J 50(3):426–441. https://doi.org/10.1007/s40098-019-00369-3
52. Shack DH, Reynolds WC (1991) Application of particle tracking velocimetry to the cyclic variability of the pre-combustion flow field in a motored axisymmetric engine. SAE Trans 100:705–717. https://doi.org/10.4271/910475
53. Sheng J, Meng H, Fox R (2000) A large eddy PIV method for turbulence dissipation rate estimation. Chem Eng Sci 55(20):4423–4434. https://doi.org/10.1016/S0009-2509(00)00039-7
54. Shrivastava AK, Jain D, Vishwakarma S (2016) Frictional resistance of drilling fluids as a borehole stabilizers. Int J Geo Eng 7(1):12. https://doi.org/10.1186/s40703-016-0026-7
55. Stanier SA, Blaber J, Take WA, White DJ (2016) Improved image-based deformation measurement for geotechnical applications. Can Geotech J 53(5):727–739. https://doi.org/10.1139/cgj-2015-0253
56. Taib SNL, Hung LS, Kolay PK (2012) Particle Image Velocimetry (PIV) analysis via MatPIV for measuring displacement of shallow foundation on uniform sand. Proceedings of 8th Asia Pacific Structural Engineering and Construction Conference & 1st International Conference on Civil Engineering Research.
57. Terzaghi K (1943) Theoretical soil mechanics. John Wiley & Sons Inc, New Jersey
58. Thielicke W, Stamhuis E (2014) PIVlab–towards user-friendly, affordable and accurate digital particle image velocimetry in MATLAB. J Open Res Softw. https://doi.org/10.5334/jors.bl
59. Tomlinson M, Woodward J (2014) Pile design and construction practice. CRC Press, Boca Raton
60. Vesić AS (1963) Bearing capacity of deep foundations in sand. Highway Res Rec 39(39):112–153
61. Vesić AS (1972) Expansion of cavities in infinite soil mass. J Soil Mech Found Div 98(3):265–290. https://doi.org/10.1061/JSFEAQ.0001740
62. Vesić AS (1977) Design of pile foundations (Vol. 42). Transportation Research Board, National Research Council, U.S.
63. White D, Take W, Bolton M (2003) Soil deformation measurement using particle image velocimetry (PIV) and photogrammetry. Géotechnique 53(7):619–631. https://doi.org/10.1680/geot.2003.53.7.619
64. White D, Take W, Bolton M, Munachen S (2001) A deformation measurement system for geotechnical testing based on digital imaging, close-range photogrammetry, and PIV image analysis. Proceedings of the International Conference on Soil Mechanics and Geotechnical Engineering, AA Balkema Publishers, 539–542.
65. Zhou M, Wang ZF, Wang SW (2011) Non-linear finite element analysis of squeezed branch pile. Adv Mater Res 243–249:2409–2414. https://doi.org/10.4028/www.scientific.net/AMR.243-249.2409

Publisher's Note